Journal of
Manufacturing and Materials Processing

MDPI

Article

Influence of Deposition Strategy and Fiber Alignment on the Mechanical Anisotropy of Short-Fiber-Reinforced Polyamide Manufactured by Additive Manufacturing Material Extrusion

Andrea Colucci [1,2], Manuela Galati [1,2,*] and Luca Iuliano [1,2]

[1] Department of Management and Production Engineering, Politecnico di Torino, 10129 Torino, Italy; andrea_colucci@polito.it (A.C.); luca.iuliano@polito.it (L.I.)
[2] Additive Manufacturing Interdepartmental Center (IAM@POLITO), Politecnico di Torino, 10129 Torino, Italy
* Correspondence: manuela.galati@polito.it; Tel.: +39-0110904569

Abstract

Short-fiber-reinforced composites (SFRCs) are widely used for their high strength-to-weight ratio. In the Additive Manufacturing (AM) field, Material Extrusion (MEX) processes inherently induce anisotropy, primarily due to fiber alignment along the deposition path, making printing direction and layer orientation critical for mechanical performance. In this study, specimens made of Onyx®, a carbon short-fiber-reinforced polyamide, were fabricated by varying their orientation on the build platform, thereby producing different infill deposition directions. Each replica contained 25 layers. Two deposition strategies were investigated: a conventional alternating ±45° raster pattern and a 0°/90° configuration. Owing to the odd number of deposited layers, the latter resulted in two distinct stacking configurations, namely *0°/90°* and *90°/0°*, depending on the orientation of the first deposited layer. With such a strategy, it was possible to obtain configurations with a predominance of fibers either aligned with or transverse to the loading direction, depending on the orientation of the first-deposited layer. Mechanical test results were systematically compared to evaluate the influence of deposition strategy and fiber orientation on tensile performances. The effect of extrusion on fiber alignment was evaluated using Scanning Electron Microscopy (SEM). Mechanical behavior was evaluated using replicated tensile testing (five specimens per condition) and SEM-based fiber-orientation analysis. The investigation confirms the anisotropic nature of MEX-produced SFRCs. In particular, the *0°/90°* configuration showed reductions of approximately 24% in tensile strength and 58% in elongation at break compared with the *±45°* configuration. These results demonstrate that both extrusion-induced fiber orientation and layer-wise deposition strategy play a crucial role in defining the mechanical response of the material.

Keywords: 3D printing; additive manufacturing; carbon composites; composites; extrusion; polyamide; polyamide composites; short-fiber composites

Check for updates

Academic Editor: Andrejs Kovalovs

Received: 6 May 2026
Revised: 5 June 2026
Accepted: 14 June 2026
Published: 16 June 2026

1. Introduction

Composite materials are, by definition, materials produced by two or more constituents (namely the phases), generally distinguished as matrix and reinforcement(s), combined at a macroscopic level [1,2]. As regards the matrix, the so-called Polymer Matrix-Based Composites (PMCs) are particularly relevant for engineering applications [3] and consist of a polymeric matrix, either thermoset or thermoplastic, where a reinforcing phase is embedded [4]. Reinforcements can be classified based on their dimensions into short fibers, continuous fibers, or particles ranging in size from nanometers to a few millimeters [5].

Short-fiber-reinforced composites (SFRCs) are materials in which the reinforcing phase consists of discontinuous fibers of a certain length, typically with a relatively low length-to-diameter aspect ratio, and the fibers are randomly dispersed into the matrix [6]. Their mechanical behavior is generally isotropic in the plane (and, consequently, orthotropic in the out-of-plane direction) if the reinforcing phase is equally distributed all over the ply [7]. In conventionally manufactured SFRCs, stacking multiple plies with approximately homogeneous fiber distributions usually results in an almost-isotropic response [2,8,9].

Composite components can be produced using many different methods, depending mainly on the material, component size, and production volume [5]. Among these processes, Additive Manufacturing (AM), also known commercially as 3D printing, is a viable option. AM techniques refer to a set of processes based on the automated deposition of successive layers of material to create a three-dimensional object, starting from 3D CAD models [10]. However, owing to the layered nature of the techniques, AM components could show anisotropic behavior along the build direction [11,12].

According to the ASTM 52900:2021 standard [13], AM processes can be classified into seven distinct categories, based on their characteristics. A brief description of the available AM techniques today for producing composites with the corresponding matrix and fiber [5,14,15] is summarized in Table 1.

Table 1. Main AM technologies suitable for producing composite materials.

AM Technology	Description	Type of Polymeric Matrix Used	Type of Fiber Reinforcement Used
Powder bed fusion laser beam (PBF-LB/P)	Focused laser source used to locally sinter and melt the material	Thermoplastic powders (usually polyamides)	Short fibers to nanoparticles mixed in the powder
Vat photopolymerization (VPP)	Focused laser source or UV projection to locally polymerize the material	Thermoset liquid resins	Small particles suspended in the resin
Binder jetting (BJT)	Selective drop of thermoset binding agent to solidify the material	Thermoplastic powders	Short fibers to nanoparticles mixed in the powder
Material Extrusion (MEX)	Extrusion of the material through a heated nozzle along a selected path	Thermoplastic filaments	Short fibers to nanoparticles dispersed in the filament. Long, continuous fibers pre-impregnated into a bonding matrix (CFF, [16])

Among the technologies reported in Table 1, MEX is certainly the most widely used, thanks to its relative simplicity, low cost, and capability to produce environmentally friendly, "green" composites [17]. MEX techniques also enable the manufacture of high-performance materials, also known as technopolymers (e.g., PEEK [18]). Among AM processes for composite, MEX processes are the only ones capable of producing composites with long-fiber reinforcement, enabled by a technology variant known as Continuous Filament Fabrication (CFF, patented by Markforged®, [19]). With respect to the common MEX processes, CFF implies an extrusion head equipped with two nozzles and a cutter. A nozzle is dedicated to depositing matrix material. The second nozzle is dedicated to depositing a filament comprising a bundle of continuous fibers pre-impregnated with a bonding polymer. At the end of the reinforcement extrusion path, the cutter cuts the filament. The commercially available reinforcement filaments are carbon, glass, and Kevlar, while the matrix can be a pure thermoplastic polymer such as TPU, PLA, or PA [17], or a carbon short-fiber-reinforced polyamide called Onyx® [20], as patented by Markforged® [19]. A detailed description of the CFF process can be found in [5,16]. Owing to its increasing use, Onyx® has been investigated using techniques such as pyrolysis, thermogravimetric analysis (TGA), and scanning electron microscopy. These analyses determined a solid load slightly above 10% in volume [21] or ~15% by weight [22], and chopped fibers with a diameter of roughly 7–8 μm [21,23,24]. On the other hand, the analysis of the mechanical behavior of Onyx is also a hot research topic from both experimental and simulation [25,26] perspectives. In particular, experimental topics include the investigation of processing parameters [18,23,27], environmental conditions [28,29], mesostructured properties [30], and reinforcing strategy [22,27,31]. The main applications today are metal replacement (e.g., aluminum components) in fields requiring high weight-to-strength ratios (e.g., aerospace and automotive), such as cores for lightweight sandwich structures [32,33]. The increasing interest in the use of Onyx® is due not only to its mechanical performance but also to the simplicity of CFF production, lower production costs, and environmental benefits compared with producing metallic components. On the other hand, better material use requires a deep understanding, particularly given the peculiarities of material formation through extrusion. As mentioned above, for SFRCs, the short fibers should not exhibit any preferential orientation. However, as observed by Mulholland et al., the extrusion process resulted in some fiber alignment, with fibers oriented parallel to the extrusion direction [34]. Similar observations were also reported by Canegrati et al. [30], highlighting the influence of the manufacturing process on the internal mesostructure of MEX-produced short-fiber-reinforced composites. Nevertheless, quantitative investigations that directly correlate microscale fiber-orientation measurements with the tensile response of specimens manufactured with different deposition configurations remain limited. Therefore, the relationship between the preferential orientation of short fibers with the deposited filaments and the resulting in-plane mechanical anisotropy is still only partially understood. Together with the orientation of the extrusion path relative to the loading direction, fiber alignment within the deposited filament may significantly contribute to the overall mechanical response of the material, leading to behavior that differs from the conventional assumption of randomly distributed fibers and, consequently, orthotropic but in-plane isotropic properties.

The present work is based on the hypothesis that the extrusion process induces a preferential alignment of short carbon fibers along the deposition direction and that this alignment contributes significantly to the in-plane mechanical anisotropy of MEX-produced Onyx®. To test this hypothesis, specimens were manufactured with different deposition configurations relative to the loading direction and characterized by tensile testing and SEM. The objective was to establish a direct relationship between extrusion-induced fiber orientation and the resulting mechanical response. The production was carried out on a Markforged® MarkTwo™ system. Owing to the machine's closed-source software, direct control over material orientation is not possible; instead, fiber alignment within the printed specimens is obtained by rotating the sample relative to the machine's default deposition orientation.

2. Materials and Methods

2.1. Machine Description

All specimens in this work were produced using the Markforged® MarkTwo™ desktop printer (Markforged Holding Corporation, Waltham, MA, USA). The material used is Markforged's Onyx® (Markforged Holding Corporation, Waltham, MA, USA), a polyamide matrix reinforced with short carbon fiber [19,20]. The fiber volume fraction for Onyx® is reported to be ~10% [21]. The proprietary software, Eiger™ (Version: 3.20), manages the entire process, including slicing.

In the software, the main printing parameters, such as extrusion speed, extrusion temperature, and infill angle, are preset and inaccessible to the user, limiting direct control over the manufacturing process. The scientific literature reports printing speeds computed from an extrusion volume rate of ~7 cm^3/h [16,35]. The layer thickness was set at 0.125 mm; the infill type was selected as "solid", corresponding to a fully dense infill; and one contour wall was selected. This represents the minimum contour configuration permitted by the Eiger™ software and was adopted to maximize the contribution of the infill region to the mechanical response. The machine is equipped with a nozzle for matrix extrusion with a diameter of 0.200 mm. The extrusion temperature, as monitored by the machine's thermocouple, was 270 °C [16].

The infill angle cannot be defined by the user, as the Markforged® MarkTwo™ extrudes the matrix material in an alternating +45°/−45°/+45°/... pattern relative to the main machine axes (i.e., along the print bed diagonals). To obtain different fiber orientations, each sample was positioned by rotating it relative to the extrusion head movement, as explained in the next paragraph.

2.2. Preliminary Characterization

To evaluate and quantify the fiber alignment with respect to the printing deposition path direction, a single layer of material was printed on the substrate and analyzed using scanning electron microscopy (SEM) [36], using a JEOL JCM-6000plus [37] benchtop microscope (JEOL Ltd., Tokyo, Japan). The sample had a thickness of 0.125 mm (corresponding to a single layer) and overall dimensions of 50×20 mm^2. After production, the sample was cut into smaller squares with sides of approximately 10 mm, which were then coated with elemental platinum (Pt) to enhance electrical conductivity, using a Quorum Q150TS [38] turbomolecular-pumped sputter coater system (Quorum Technologies Ltd., Laughton, UK). The sputtered-layer thickness was around 10 nm. The sputtered samples were subsequently mounted onto conductive bases using double-sided tape and scanned at an acceleration voltage of 5 kV and at a magnification of ×200 under high vacuum.

Images were processed using the software ImageJ (Version: 1.54g) to evaluate fiber alignment using the distribution of the misorientation angles, $|\alpha_i - \alpha_0|$; Hermans orientation parameter; and the second-order Advani–Tucker tensor.

Average orientation, $\boldsymbol{\alpha}$, was subsequently computed as follows (1):

$$\boldsymbol{\alpha} = (\Sigma_i^{\,n} |\alpha_i - \alpha_0|)/n \quad (1)$$

where n is the total number of analyzed fibers, while "α_i" is the orientation of the i-th single fiber with respect to the global extrusion direction, α_0, determined with a preliminary scanning performed at a lower (×22) magnification, by measuring the angle of the visible extrusion raster patterns. Ten independent measures were performed at different locations across the specimen, and the mean values were adopted as the reference extrusion direction, α_0. Standard deviations of measured angles were below 1°.

The Hermans orientation parameter, f [39], is calculated as follows (2):

$$f = (3 \times \langle cos^2\theta_i \rangle - 1)/2 \quad (2)$$

where "θ_i" is the angle between the fiber and the reference direction, which is assumed to be the extrusion direction. Therefore, θ_i is equal to $|\alpha_i - \alpha_0|$. The Hermans orientation parameter provides a scalar measure of fiber alignment. Its value ranges from −0.5 for fibers oriented perpendicular to the reference direction, to 0 for a random orientation, and to

1 for perfectly aligned fibers. Consequently, values approaching 1 indicate an increasingly pronounced preferential orientation along the reference direction.

The second-order Advani–Tucker tensor, $\boldsymbol{A}$ [40], provides a statistical description of the fiber orientation state within the analyzed plane, which, in this case, is assumed to be the extrusion plane, and it is calculated as follows (3):

$$\boldsymbol{A} = (1/n)\Sigma_{i^n}\begin{bmatrix} cos^2\theta_i & sin\theta_i cos\theta_i \\ sin\theta_i cos\theta_i & sin^2\theta_i \end{bmatrix} \quad (3)$$

The diagonal components quantify the degree of alignment along the corresponding coordinate directions and satisfy the condition that their sum equals 1. For a completely random in-plane fiber distribution, the diagonal terms are equal to 0.5, whereas values approaching 1 indicate an increasingly pronounced preferential alignment along the corresponding direction. Thus, a dominant component along the extrusion direction reflects strong extrusion-induced fiber orientation.

2.3. Tensile Specimen Design

Dog-bone-shaped tensile specimens were designed according to the ASTM D638 Type II standard [41]. Specimens' dimensions were slightly modified, within the standard's range, to accommodate the characteristics of the production technology, as already outlined by Galati et al. [25]. Therefore, the overall dimensions of the specimens, as shown in Figure 1, are 185 × 19 × 3.125 mm^3 (length × width × thickness), with a calibrated trait width of 6.1 mm. Using a fixed layer thickness of 0.125 mm, 25 layers were obtained.

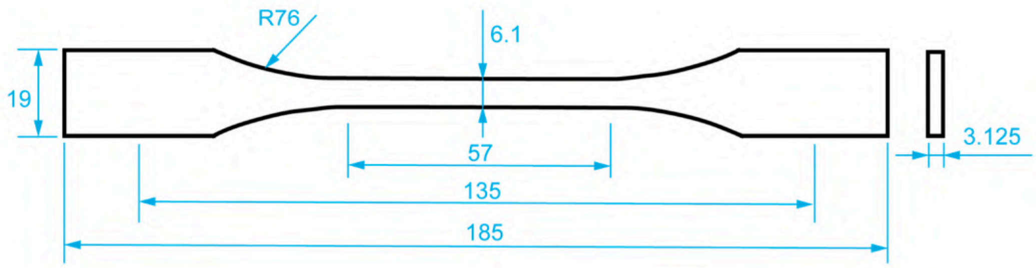

Figure 1. ASTM D638 Type II tensile specimen geometry and dimensions designed according to Galati et al. [25].

In Eiger™, the samples were positioned with the larger surface parallel to the *x*-*y* plane (see Figure 2) and attached to the printing bed. To obtain different infill orientations, the samples were opportunistically rotated around the building direction (*z*-axis in Figure 2), orienting their load direction (i.e., the main dimension of the specimens) with respect to the extrusion head movement, which is automatically set as an alternating +45°/−45°/+45°/... angle with respect to the *x*- or *y*-axis. This allowed for the production of specimens in which the infill has various angles and stacking sequences relative to the tensile load direction.

Given the hypothesis that the extrusion process tends to align fibers in the deposition direction, the different rotations of the sample were aimed at obtaining specimens with short fibers, dispersed in the matrix filament, aligned differently (either parallel, transverse, or at 45°) relative to the extrusion direction.

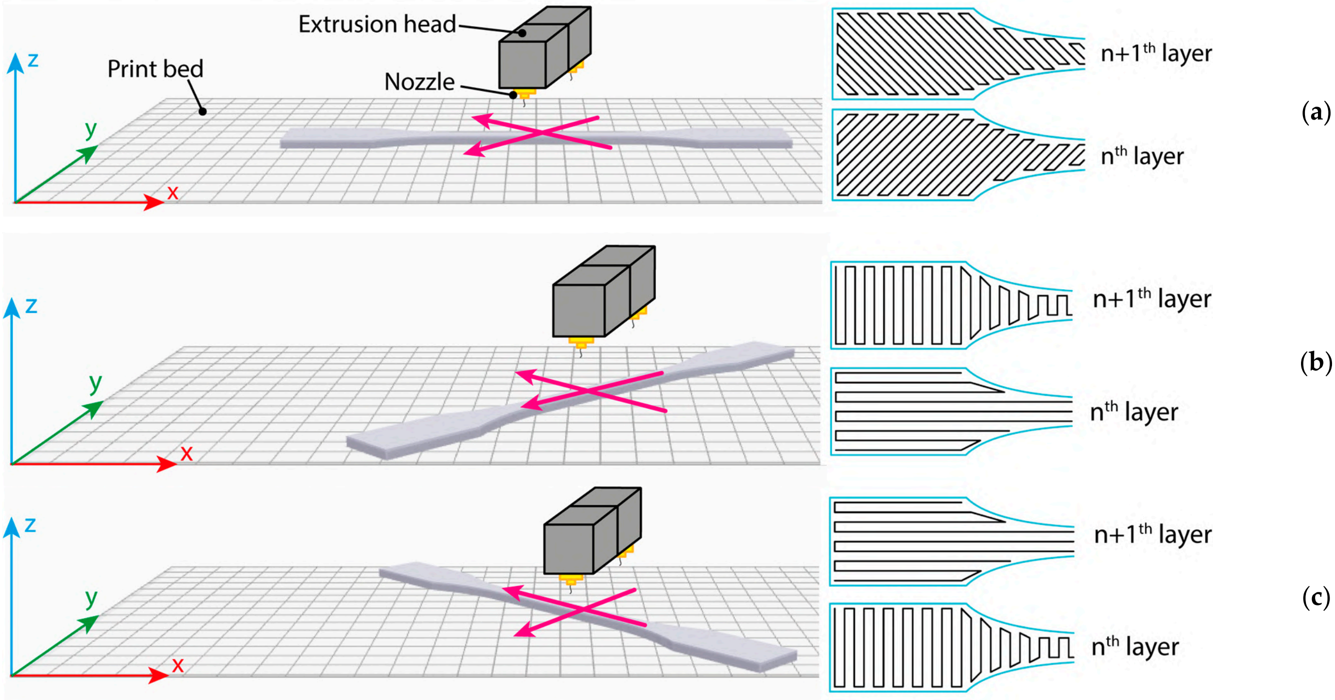

Figure 2. On the left, the specimen positioning on the build plate for each configuration. The rotation is around the *z*-axis (shown in blue). The magenta arrows mark the extrusion directions. On the right, the infill patterns for the printed specimens. The black lines represent the infill, and the light blue one is the contour. (**a**) Positioning and infill used for the *±45°* specimens. (**b**) Positioning and infill used for the *0°/90°* specimens. (**c**) Positioning and infill used for the *90°/0°* specimens.

Using a 0° rotation angle around the *z*-axis, specimens were printed with a +45°/−45°/+45°/... stacking alternance, as shown in Figure 2a. These specimens will be referred to as "*±45°*". By rotating the specimens either +45° or −45° around the *z*-axis with respect to *±45°* (Figure 2b,c), both a 0°/90°/0°/... and a 90°/0/90°/... stacking sequence were achieved. Given that the specimens are built with an odd (25) number of layers, these stacking sequences resulted either in specimens with 13 layers along the load direction and 12 transverse to it (named "*0°/90°*", Figure 2b) or specimens with 12 layers along the load direction and 13 transverse to it (named "*90°/0°*", Figure 2c).

2.4. Tensile Specimen Testing

Tensile specimens were 3D-printed, one at a time (with a printing time of approximately 60 min), and tested within 5 min of removal from the build plate. This interval corresponded only to the time required for specimen handling, visual inspection, mounting in the testing machine, and test setup, thereby minimizing and standardizing environmental moisture exposure before testing [42]. Five replicas for each investigated condition were tested, according to the reference standard [41]. Tests were carried out using an electro-mechanical universal tensile testing machine, EASYDUR ITALIANA AURA 10T (EASYDUR S.r.l., Arcisate, Italy) [43]. Tensile tests were conducted at 5 mm/min, as prescribed by the standard [41], and data were recorded at a sampling rate of 500 Hz. Load was acquired by the machine's 10 kN load cell, and the crosshead displacement was measured with a resolution of 0.001 mm.

Load–displacement curves were generated using an adapted MATLAB® code (Version: 24.2.0.3070828 (R2024b) Update 7), developed for importing and analyzing the output files generated by the tensile testing machine to obtain standard stress-strain (σ-ε) curves and, consequently, tensile strength and elongation at break values. Tensile modulus, E_t, was calculated according to the ISO 527-1 [44] standard as follows (4):

$$E_t = d\sigma/d\varepsilon \tag{4}$$

where $d\sigma/d\varepsilon$ is the slope of a regression line fitted in the curve range $0.0005 \leq \varepsilon \leq 0.0025$.

2.5. Fractographic SEM Analysis

Failure surfaces were analyzed to determine the nature of the rupture mechanism using a TESCAN MIRA 3 [45] FESEM (TESCAN GROUP, a.s., Brno, Czech Republic), working under high vacuum, and applying an acceleration potential of 5–8 kV. Samples from rupture surfaces of ±*45*°, *0*°/*90*°, and *90*°/*0*° specimens, cut at approximately 10 mm from the breaking point, were sputtered with elemental platinum (Pt) to enhance electrical conductivity using an Agar Scientific High-Resolution Coater 208HR (Agar Scientific Ltd., Stansted, UK) [46]. The Pt coating was approximately 10 nm thick. The two halves of the rupture surfaces were positioned to image either the lateral or the frontal view of the breakage.

3. Results and Discussion

Results of the tensile tests conducted in accordance with ASTM D638 [41] are reported here. All tested specimens failed within the gauge section. No failures occurred at the grips or outside the calibrated length. As mentioned above, tensile strength, σ_{max} (i.e., the maximum stress value reached during the test); elongation at break, ε_f (i.e., the maximum strain value reached prior to failing); and tensile modulus, E_t, are determined for each tested sample. Averages and standard deviations are reported in Table 2 for the ±*45*°, *0*°/*90*°, and *90*°/*0*° cases, and are compared in Figure 3 as a bar graph.

Table 2. Tensile strength, σ_{max}; elongation at break, ε_f; and tensile modulus, E_t, for the tested infill orientation cases (±*45*°, *0*°/*90*°, and *90*°/*0*°): averages and standard deviations.

Mechanical Properties	±45°	0°/90°	90°/0°
Tensile strength, σ_{max} [MPa]	44.08 ± 1.17	33.31 ± 1.15	40.82 ± 1.26
Elongation at break, ε_f [%]	14.35 ± 0.68	6.09 ± 0.51	10.06 ± 0.37
Tensile modulus, E_t [GPa]	2.29 ± 0.25	2.17 ± 0.11	2.28 ± 0.14

Among the investigated stacking configurations, the ±*45*° specimens exhibited the best overall performance, combining the highest tensile strength (44.08 MPa), elongation at break (14.35%), and tensile modulus (2.29 GPa). In contrast, both the *0*°/*90*° and *90*°/*0*° cases showed reductions in all measured properties, with the *0*°/*90*° configuration being the most affected.

Average tensile test curves (obtained by averaging the five replica curves up until the first failure elongation of the batch) are shown in Figure 4.

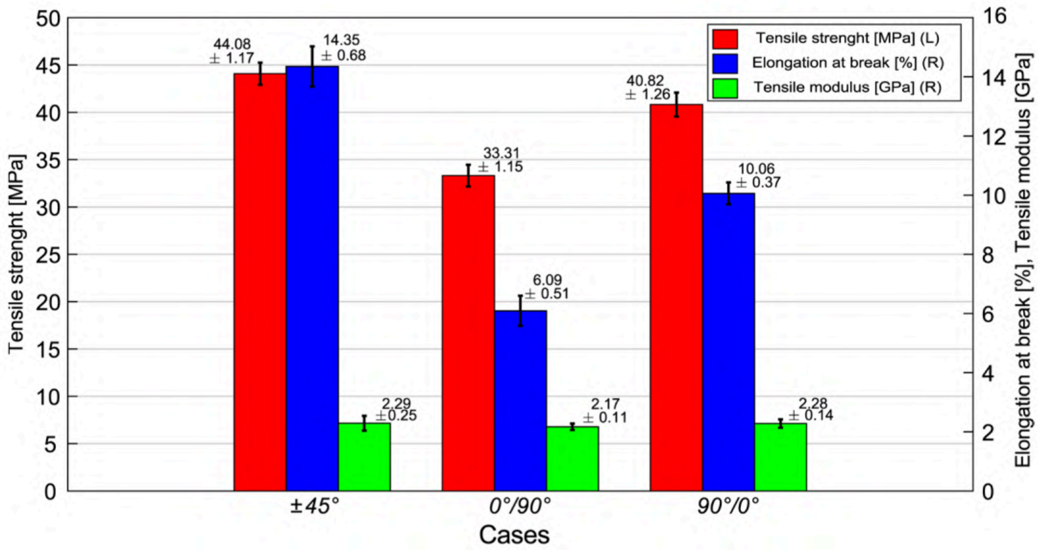

Figure 3. Tensile strength, σ_{max}; elongation at break, ε_f; and tensile modulus, E_t, for the tested infill orientation cases (±*45*°, *0*°/*90*°, and *90*°/*0*°): averages and standard deviations.

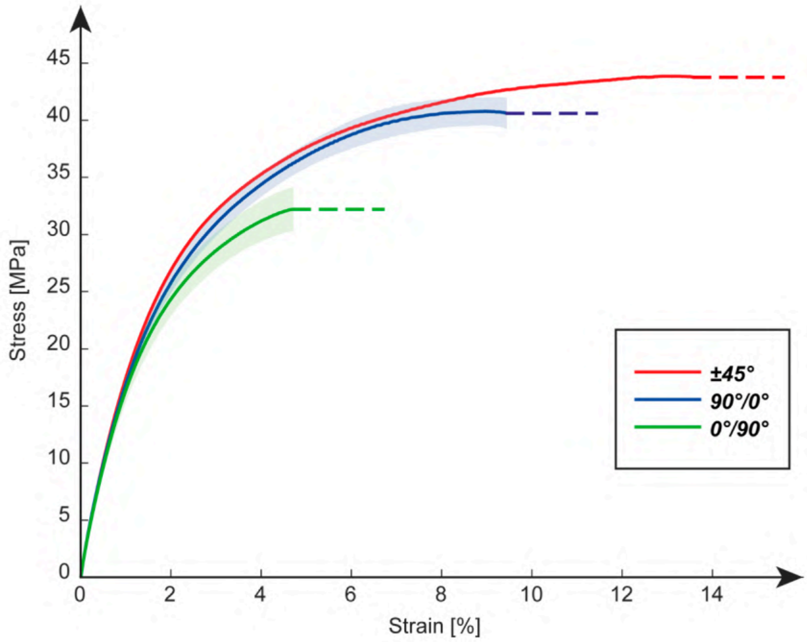

Figure 4. Average tensile test curves for the ±*45*°, *0*°/*90*°, and *90*°/*0*° cases. The shaded area represents ±1 standard deviation calculated from the curves obtained from the five replicas. Average curves are reported up to the first-failure elongation for each batch.

The tensile curves and average values showed a remarkable decrease in mechanical response compared with the ±*45*° infill for both the *90*°/*0*° and *0*°/*90*° cases. In particular, the latter showed a greater decrease, with elongation at break reduced by half and a marked decrease in tensile strength. The percentages of variation in the mechanical properties of *0*°/*90*° and *90*°/*0*° specimens, compared with the ±*45*° specimens, are reported in Table 3. The ±*45*° configuration was used as the reference condition because it exhibited the highest overall mechanical performance among the investigated cases.

Table 3. Percentages of variation in the mechanical properties caused by the different infilling cases. The ±45° configuration is used as the reference condition because it exhibited the highest overall mechanical performance among the investigated cases.

Mechanical Properties	Variation 0°/90° vs. ±45°	Variation 90°/0° vs. ±45°
Tensile strength, σ_{max}	−24%	−7.4%
Elongation at break, ε_f	−58%	−30%
Tensile modulus, E_t	−5.2%	−0.44%

As can be observed in Table 3, the deposition pattern largely influences the mechanical outcome, and MEX applied to short-fiber-reinforced composites exhibits anisotropic behavior not only along the *z* build direction [12] but also within the *x*-*y* plane.

For the sake of completeness, pairwise comparisons between the investigated configurations were performed using Tukey's *t*-tests. A significance threshold of $\alpha = 0.05$ was adopted throughout the analysis. The analysis is reported in Appendix A. The *p*-values for tensile strength and elongation at break were below the adopted significance level ($\alpha = 0.05$), confirming statistically significant differences among the configurations investigated. Conversely, the tensile modulus showed *p*-values greater than 0.05, indicating no statistically significant differences among the three analyzed cases.

These results can be explained by the SEM analysis, an example of which is shown in Figure 5. Figure 5a shows the deposition path, with the extrusion direction highlighted in green. Figure 5b is a magnification of the previous one, in which the extrusion direction is still indicated with the green arrow, and a certain number of fibers are marked by dotted light blue lines or are bounded into the yellow boxes to facilitate the visualization.

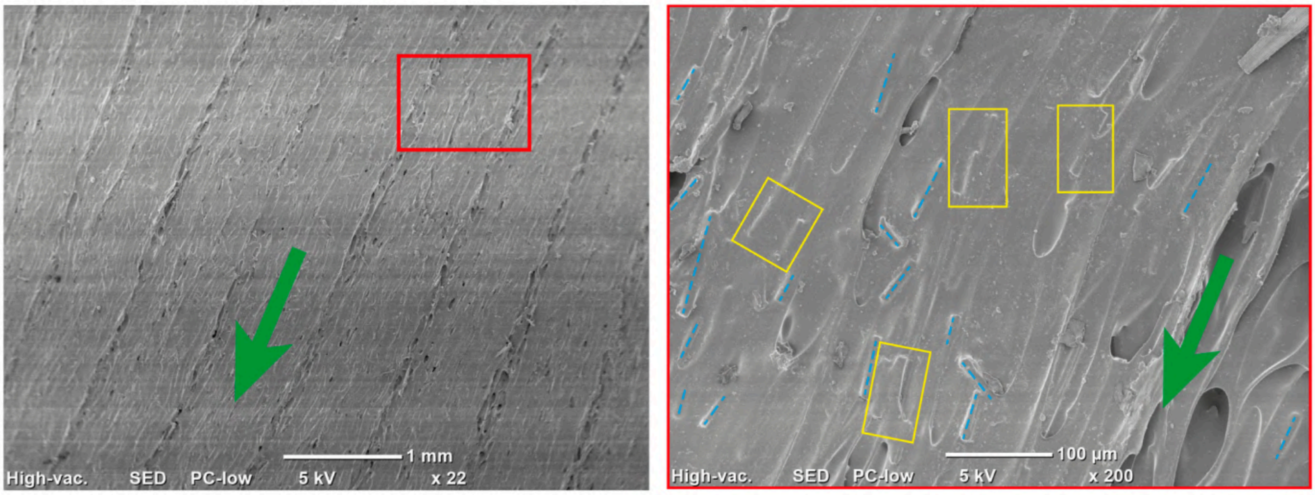

(**a**) (**b**)

Figure 5. Fiber misalignment, $|\alpha_i - \alpha_0|$, measurements: (**a**) Low-magnification (×22) image to determine the extrusion direction for the sample α_0, which is indicated by the green arrow. The red box highlights the ROI used in (**b**) for fiber angle measurements. (**b**) High-magnification image (×200) used to determine the single fibers' orientation angles, α_i. Some fibers' directions are marked by the dotted blue lines. Other fibers are bound into the yellow boxes to facilitate their visualization. For reference, the green arrow once again indicates the extrusion direction.

For each detected fiber, the orientation, α_i, with respect to the deposition direction, α_0, was measured, and the misorientation angle, $|\alpha_i - \alpha_0|$, was evaluated. The lower the misorientation angle, the more the fiber is aligned parallel to the extrusion direction. A total of 1068 fibers, measured in multiple SEM micrographs acquired from different 10 mm × 10 mm sample sections, were analyzed. The distribution of the measured

$|\alpha_i - \alpha_0|$ is shown in Figure 6, using a histogram with 11 classes having a size equal to 8.1°, as per Sturges' rule [47].

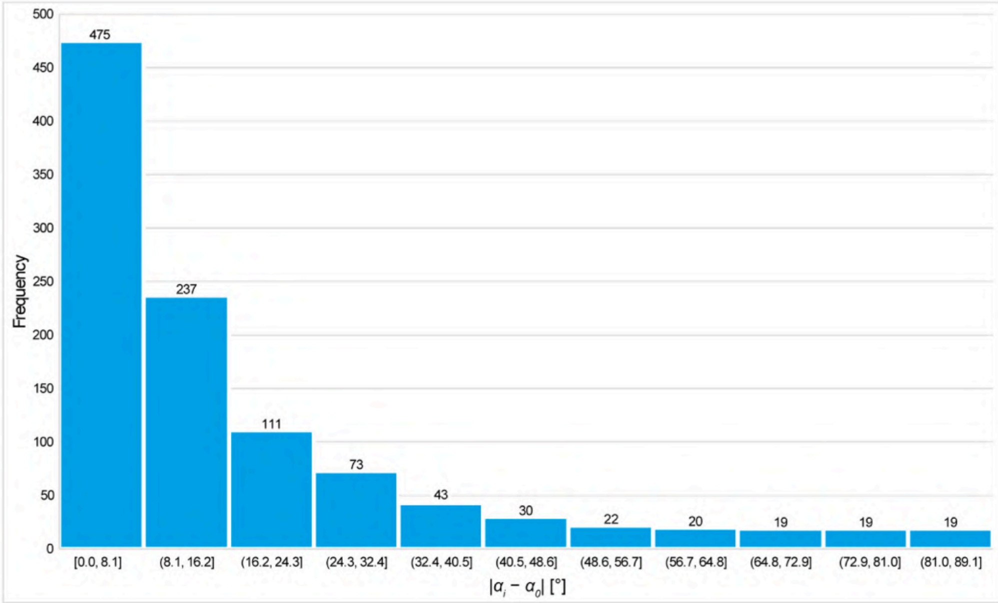

Figure 6. Distribution of misorientation angle $|\alpha_i - \alpha_0|$ for the analyzed fibers in the 0–90° range.

As can be observed in Figure 6, The minimum measured misorientation was 0.02°, while the maximum measured was 89.11°. The average angle, $\boldsymbol{\alpha}$, is equal to 17.23. The preferential orientation of the fibers corresponds to the first class of the histogram, ranging from 0.0° to 8.1°, with a class frequency of roughly 45% of the total measurements, while over 70% of the total measured fibers exhibit a misorientation angle, $|\alpha_i - \alpha_0|$, below 20°. This result indicates a preferential orientation along the extrusion direction. The Hermans parameter, calculated with respect to the extrusion direction, was 0.785, confirming a pronounced preferential alignment of the fibers along the extrusion path [48]. This observation is further supported by the second-order Advani–Tucker orientation tensor, $\boldsymbol{A}$, which was calculated as follows:

$$\boldsymbol{A} = \begin{bmatrix} 0.856 & 0.196 \\ 0.196 & 0.144 \end{bmatrix}.$$

The dominant value of the first diagonal component (A_{11} = 0.856) indicates a pronounced preferential alignment of the fibers along the reference direction, corresponding to the extrusion path. Consequently, the tensor eigenvalues were found to be $\{\lambda_{A1}, \lambda_{A2}\} = \{0.906, 0.094\}$, which approach the theoretical eigenvalue values of a perfectly aligned fibers system ($\{\lambda_1, \lambda_2\} = \{1, 0\}$) [40].

These results collectively confirm that the extrusion process induces a marked orientation of the short carbon fibers within the deposited filament, thereby affecting the final mechanical performance of the part. As a result, each deposited filament can be regarded as a locally reinforced unidirectional composite, where the reinforcement direction coincides with the printing extrusion direction. This explains how the important microstructural insight shifts into these macroscopic response variations, such as the observed reductions both in tensile strength (−24%) and elongation at break (−58%) observed in the *0°/90°* samples when compared to the ±*45°* ones (see Table 3), suggesting a more brittle mechanical behavior, while the fractographic FESEM imaging of ruptured ±*45°* specimens, shown in Figure 7, indicates a more complex, shear-dominated rupture.

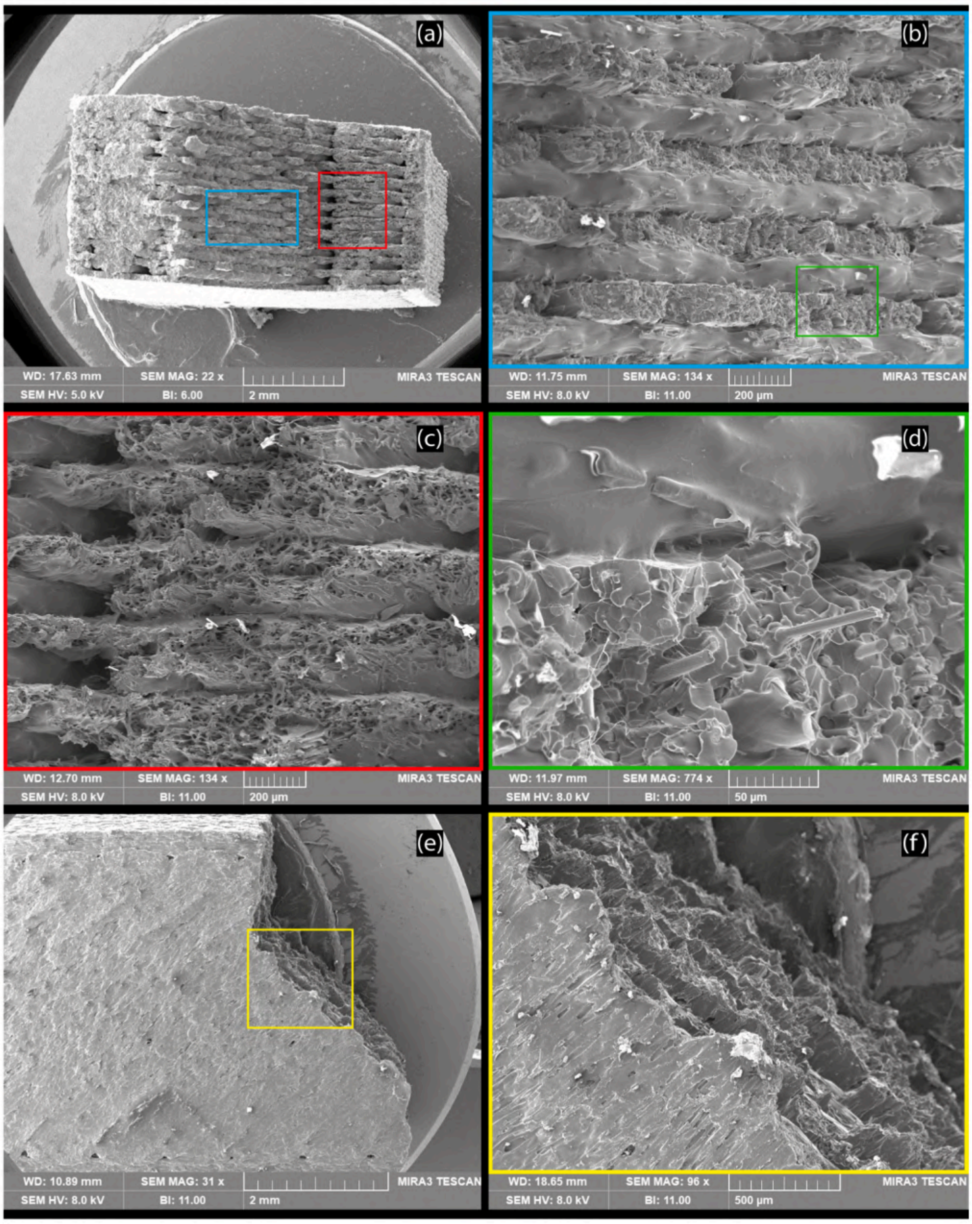

Figure 7. Fractographic FESEM images of rupture surfaces from ±*45*° specimens. Magnification and imaging parameters are reported below each image. Tensile direction is outbound from the image for (**a**–**d**), and toward the right for (**e**,**f**). Images: (**a**) 22× image of the rupture surface, front view, showing a complex S-shaped fracture surface, with the central part inclined at 45° to the tensile direction; (**b**) 134× magnification from (**a**), showing alternating fractured +45°-oriented layers and detached −45°-oriented layers; (**c**) 134× magnification from (**a**), showing the complex fracture surface present at the angle variation point of the rupture surface; (**d**) 774× magnification from (**b**), showing the detached −45°-oriented layer and the complex, shear-dominated fracture surface of the +45-oriented one, with fiber pullout visible, showing a preferential alignment of the fibers along the extrusion path; (**e**) 22× image of the rupture surface, top view, showing a complex S-shaped fracture surface, with the central part being inclined at 45° with respect to the tensile direction; and (**f**) 96× magnification from (**e**), showing the complex 45°-oriented fracture surface and fibers pulling out from it.

The macroscopic S-shaped fracture morphology can be attributed to the combined effects of the alternating ±45° raster architecture and the preferential alignment of short fibers along the extrusion direction. Since approximately 70% of the fibers have a misorientation angle below 20°, each printed layer behaved as an anisotropic reinforcement layer. During tensile loading, crack propagation was repeatedly deflected at transitions between

+45° and −45° layers, producing a stepped fracture path connected by an inclined region. This morphology is consistent with a fracture process involving significant crack deflection and shear-related deformation.

In the *0°/90°* configuration, the majority of the extruded material is oriented parallel to the tensile load, and, as a consequence, so are the fibers dispersed into the material. In contrast, in the *±45°* configuration, the majority of the filament and, therefore, the embedded fibers are oriented at a certain angle with respect to the loading direction. Under tensile loading, this configuration results in a stress state dominated by shear at the filament level, as discussed in Figure 7, thereby promoting progressive load redistribution via matrix-dominated deformation mechanisms. This configuration promotes a more progressive fracture process, consistent with the higher elongation at break observed during tensile testing. This resulted in a rupture surface very different from the *0°/90°* one, as shown in Figure 8.

As already suggested by the tensile tests' mechanical results, fractographic FESEM observations indicate a more brittle failure behavior in the *0°/90°* specimens. The fracture surfaces exhibit clean, brittle-like rupture features in the 0° layers, together with extensive fiber pullout, while the 90° layers appear predominantly detached along the tensile direction. These observations are consistent with the preferential alignment of fibers along the extrusion path. Although the material contains short fibers, their strong preferential alignment along the extrusion direction results in a pronounced anisotropic mechanical response, with a reduction in elongation at break that is consistent with trends commonly observed in unidirectionally reinforced composites. On the other hand, the reduction in tensile strength may be associated with stress concentrations arising from inter-filament voids and discontinuities between adjacent deposition paths.

The *90°/0°* configuration exhibits intermediate behavior, indicating that the stacking sequence (subordinated to the first-layer orientation) also plays a role in determining mechanical performance. Figure 9 shows the fractographic FESEM images of *90°/0°* specimens.

Although the same filament orientations as in the *0°/90°* case are present, the predominance of layers deposited transverse to the loading direction results in a different distribution of preferentially aligned fibers across the specimen thickness, explaining the intermediate behavior of *90°/0°* specimens, as indicated by mechanical testing and confirmed by fractographic imaging (Figure 9), that showed more substantial contribution to the tensile behavior from the matrix filament of 90°-oriented layers.

Interestingly, the tensile modulus shows only minor variations across the different configurations (within ~5%). This suggests that the elastic response is less affected by the investigated changes in deposition strategy than tensile strength and ductility. While the reinforcing fibers contribute significantly to the stiffness of the composite, the observed differences in fiber orientation appear to have a more pronounced effect on failure behavior than on the initial elastic response.

As a qualitative reference framework, the measured misorientation angles are consistent with the scientific literature on both short- [49] and long-fiber-reinforced [50,51] traditional composites (e.g., misorientation angles up to 7.5° reported for unidirectional prepregs), where preferential fiber alignment is known to influence mechanical behavior.

Overall, the combination of tensile testing and SEM analysis indicates that the anisotropic behavior of MEX-produced SFRCs stems from both the infill pattern orientation and microscale fiber alignment within the extruded material.

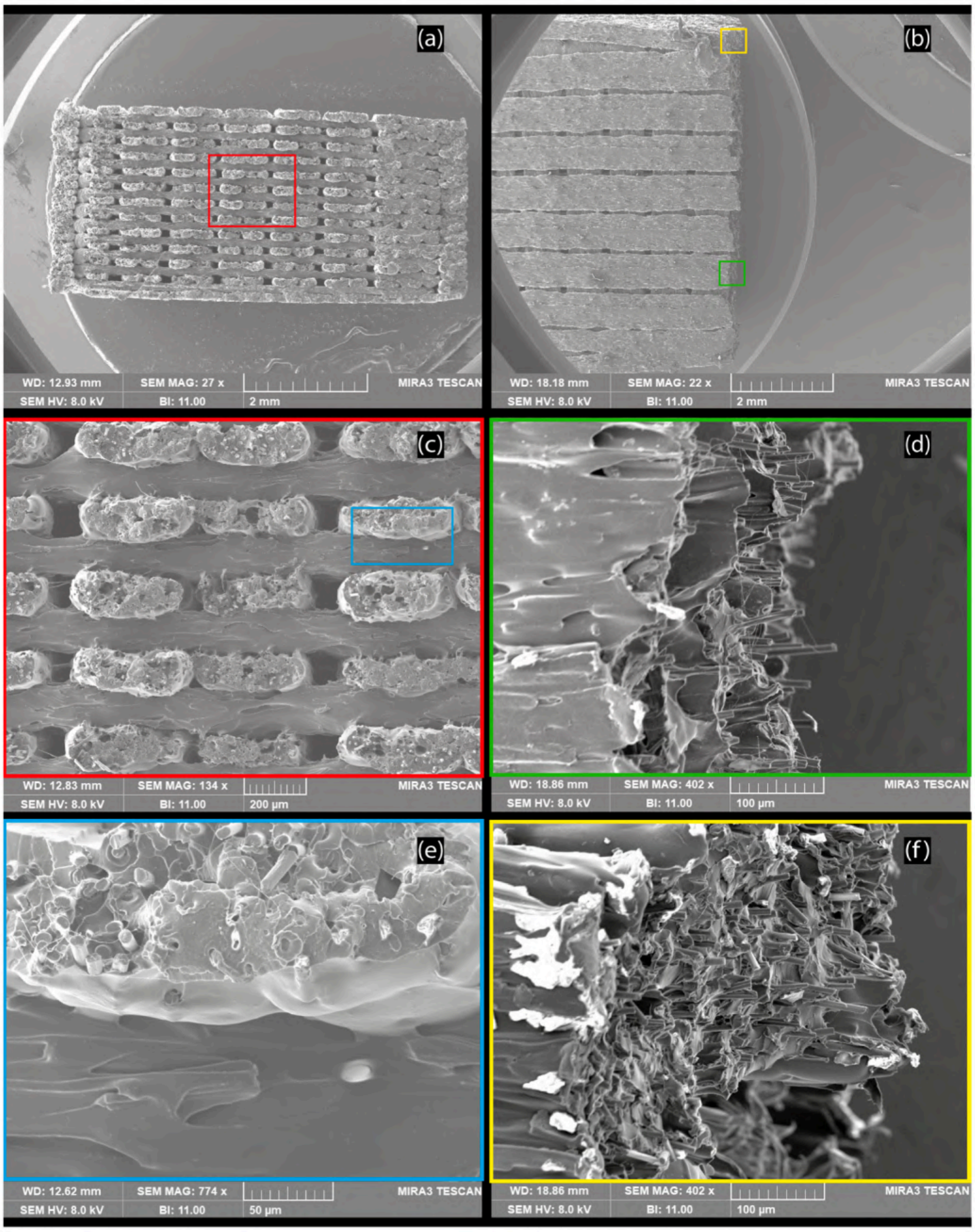

Figure 8. Fractographic FESEM images of rupture surfaces from *0°/90°* specimens. Magnification and imaging parameters are reported below each image. Tensile direction is outbound from the image for (**a**,**c**,**e**), and toward the right for (**b**,**d**,**f**). Images: (**a**) 27× image of the rupture surface, front view, showing a flat fracture surface oriented at 90° with respect to the tensile direction; (**b**) 22× image of the rupture surface, top view, showing a flat fracture surface oriented at 90° with respect to the tensile direction; (**c**) 134× magnification from (**a**), showing that the flat rupture surface consists of alternating, detached 90°-oriented layers, and 0°-oriented layers that display fracture surfaces indicative of a more brittle failure mode relative to the ±45° configuration, and inter-filament voids are visible between 0°-oriented extrusion paths; (**d**) 402× magnification from (**b**), showing straight-edged, 90°-oriented rupture surface, with fiber pullout visible, aligned along the extrusion path; (**e**) 774× magnification from (**c**), showing the rupture and fiber pullout from the 0°-oriented top layer against the detached 90°-oriented bottom layer; and (**f**) 402× magnification from (**b**), displaying the interface area between the contour (**top**) and the infill (**bottom**). Clusters of fibers aligned in the extrusion direction are visible.

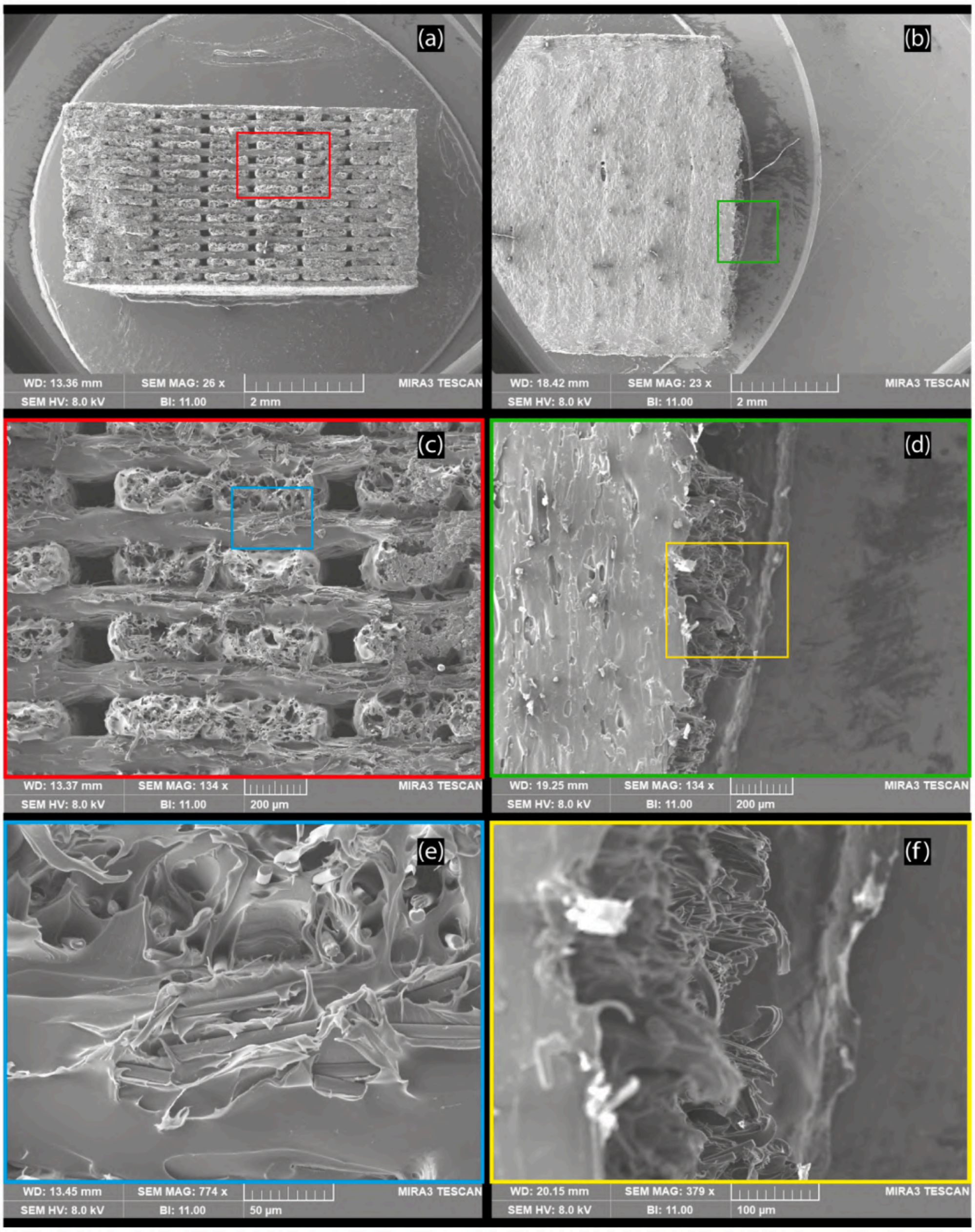

Figure 9. Fractographic FESEM images of rupture surfaces from *90°/0°* specimens. Magnification and imaging parameters are reported below each image. Tensile direction is outbound from the image for (**a**,**c**,**e**), and toward right for (**b**,**d**,**f**). (**a**) Image at 26× magnification of the rupture surface, front view, showing a generally flat fracture surface, exhibiting limited macroscopic plastic deformation, with a central part oriented at 90° with respect to the tensile direction and the lateral parts having a slight misorientation. (**b**) Image at 23× magnification of the rupture surface, top view, showing a generally flat fracture surface, exhibiting limited macroscopic plastic deformation, with a central part oriented at 90° with respect to the tensile direction and the lateral parts having a slight misorientation. (**c**) Image at 134× magnification from (**a**), showing that the flat rupture surface consists of alternating 0°- and 90°-oriented layers. The 0°-oriented layers display relatively smooth fracture surfaces with limited evidence of plastic deformation. In contrast, the 90°-oriented layers, unlike those observed in the *0°/90°* specimens (see Figure 8c), exhibit evidence of partial matrix tearing and incomplete interfacial separation, suggesting a greater involvement of matrix deformation in the fracture process. Inter-filament voids are visible between 0°-oriented extrusion paths. (**d**) Image at 134× magnification from (**b**), showing the straight-edged, 90°-oriented central part of the rupture surface. Fiber pullout is visible, further confirming that fibers are aligned along the extrusion path. (**e**) Image at 774× magnification from (**c**), showing the rupture and fiber pullout from the 0°-oriented

top layer, alongside fragments of plastically deformed and torn polymer filaments from the 90°-oriented bottom layer, exposing fibers oriented along the extrusion direction. (**f**) Image at 376× magnification from (**d**), displaying clusters of fibers aligned along the extrusion direction and torn matrix filaments, supporting the conclusion that matrix in the 90°-oriented layers had a more significant role in the fracture process.

4. Conclusions

This study investigated the effect of infill orientation on the mechanical behavior of MEX-produced SFRCs through tensile testing and SEM analysis. The main findings can be summarized as follows:

- SEM analysis revealed a strong preferential alignment of fibers along the extrusion direction, with roughly 45% of the fibers having a misorientation angle below 8.1° with respect to the extrusion direction. Compared with findings reported in the scientific literature [50,51], a misalignment angle of up to approximately 7.5° is generally considered sufficiently small to preserve a preferential orientation and can therefore still have a measurable influence on the overall material behavior.
- The ±*45*° infill configuration, consisting of alternating layers deposited at a +45°/−45° angle with respect to the tensile direction, provided the best mechanical performance, with the highest tensile strength and elongation at break among the investigated configurations. This can be explained by the fact that the fibers are oriented at 45° with respect to the load direction. In contrast, only minor differences were observed in tensile modules.
- In configurations in which the majority of layers in the specimen have a filament aligned parallel to the load direction, the material exhibits a more pronounced directional dependence of its mechanical response, consistent with the preferential orientation of the reinforcement. Therefore, the sample consisting of 13 layers oriented along the tensile direction and 12 rotated 90° with respect to it showed the most significant reduction in mechanical properties, particularly in ductility (−58%) and tensile strength (−24%), with a more brittle failure behavior, while the sample consisting of 12 layers oriented along the tensile direction and 13 rotated 90° with respect to it exhibited intermediate properties, suggesting that the predominance of differently oriented deposited filaments may contribute to the observed mechanical response.
- Infill orientation only slightly affected the tensile modulus, whereas considerably larger variations were observed in tensile strength and elongation at break. This indicates that, within the investigated configurations, deposition strategy had a more pronounced influence on strength and ductility than on the initial elastic response.
- The observed anisotropy in mechanical behavior is the result of the combined effect of filament orientation and fiber alignment induced by the extrusion process.

These findings confirm the original hypothesis that the mechanical performance of MEX-processed SFRCs is highly anisotropic, not only along the build direction but also within the deposition plane. The methodology adopted for correlating fiber orientation and mechanical response can be readily extended to other MEX systems, materials, and reinforcement types. More generally, optimizing infill strategies to appropriately orient Material Extrusion with respect to the principal loading directions is crucial for maximizing structural performance. Future work could extend the present investigation through three-dimensional microstructural characterization and advanced strain measurement techniques.

Results from this research line are significant for both the design of 3D-printed SFRCs structures and their numerical modeling. In particular, the extrusion direction is a key parameter that must be carefully considered during the design phase, as it influences fiber orientation and, consequently, the material's mechanical response. Furthermore, the quantitative fiber-orientation information obtained in this work may provide useful input for future micromechanical and finite element modeling (FEM) approaches to describe the anisotropic behavior of MEX-produced short-fiber-reinforced composites. Beyond conventional FEM approaches, recent developments in artificial intelligence and machine learning have demonstrated promising capabilities for linking processing conditions, microstructural evolution, and mechanical performance in additively manufactured composites. The integration of experimentally measured fiber-orientation descriptors with data-driven modeling frameworks may therefore represent an interesting direction for future research [52,53].

Author Contributions: Conceptualization, A.C. and M.G.; methodology, A.C. and M.G.; software, A.C.; validation, A.C. and M.G.; formal analysis, A.C.; investigation, A.C.; resources, L.I.; data curation, A.C.; writing—original draft preparation, A.C.; writing—review and editing, M.G. and L.I.; visualization, A.C.; supervision, M.G. All authors have read and agreed to the published version of the manuscript.

Funding: This research received no external funding.

Data Availability Statement: The raw data supporting the conclusions of this article will be made available by the authors upon request.

Acknowledgments: The authors would like to express their gratitude to Giovanni Ferrero for his assistance with the experimental work and to Giovanni Rizza for his support in SEM and FESEM imaging.

Conflicts of Interest: The authors declare no conflicts of interest.

Abbreviations

The following abbreviations are used in this manuscript:

3D	Three-dimensional
AM	Additive Manufacturing
ANOVA	Analysis of Variance
CAD	Computer-Aided Design
CFF	Continuous Filament Fabrication
FEM	Finite element modeling
FESEM	Field-Emission Scanning Electron Microscope
MEX	Material Extrusion
PMC	Polymer Matrix-Based Composite
ROI	Region of Interest
SEM	Scanning Electron Microscope
SFRC	Short-fiber-reinforced composite

Appendix A

Appendix A reports the results of ANOVA, followed by Tukey's post hoc tests (Tables A1–A3), performed for all configurations investigated in this study and for tensile strength (σ_{max}), elongation at break (ε_f), and tensile modulus (E_t). All statistical analyses were conducted using a significance level of $\alpha = 0.05$. These tests were used to assess whether differences between pairs of configurations were statistically significant. Separate analyses were performed for each mechanical property. Two configurations were considered statistically different when the adjusted p-value was below the significance level ($\alpha = 0.05$).

Table A1. Tukey's test results for tensile strength, σ_{max}, values. All tests were performed at a confidence level of α = 0.05. Couples are statistically different if the adjusted *p*-value is below 0.05.

Difference of Levels	Difference of Means	SE of Difference	95% CI	Adjusted *p*-Value
0°/90° vs. *±45°*	−10.775	0.723	(−12.683; −8.867)	0.000
90°/0° vs. *±45°*	−3.259	0.723	(−5.167; −1.351)	0.002
90°/0° vs. *0°/90°*	7.516	0.756	(5.523; 9.509)	0.000

Table A2. Tukey's test results for elongation at break, ε_f, values. All tests were performed at a confidence level of α = 0.05. Couples are statistically different if the adjusted *p*-value is below 0.05.

Difference of Levels	Difference of Means	SE of Difference	95% CI	Adjusted *p*-Value
0°/90° vs. *±45°*	−8.259	0.333	(−9.137; −7.382)	0.000
90°/0° vs. *±45°*	−4.295	0.333	(−5.173; −3.418)	0.000
90°/0° vs. *0°/90°*	3.964	0.348	(3.047; 4.881)	0.000

Table A3. Tukey's test results for tensile modulus, E_t, values. All tests were performed at a confidence level of α = 0.05. Couples are statistically different if the adjusted *p*-value is below 0.05.

Difference of Levels	Difference of Means	SE of Difference	95% CI	Adjusted *p*-Value
0°/90° vs. *±45°*	−0.125	0.112	(−0.421; 0.171)	0.521
90°/0° vs. *±45°*	−0.011	0.112	(−0.307; 0.285)	0.994
90°/0° vs. *0°/90°*	0.114	0.117	(−0.195; 0.423)	0.606

References

1. Lubin, G. *Handbook of Composites*; Springer Science & Business Media: Berlin/Heidelberg, Germany, 2013; p. 788. Available online: https://books.google.com/books/about/Handbook_of_Composites.html?hl=it&id=ct_vBwAAQBAJ (accessed on 13 April 2026).
2. Hsissou, R.; Seghiri, R.; Benzekri, Z.; Hilali, M.; Rafik, M.; Elharfi, A. Polymer composite materials: A comprehensive review. *Compos. Struct.* **2021**, *262*, 113640. [CrossRef]
3. Oladele, I.O.; Omotosho, T.F.; Adediran, A.A. Polymer-Based Composites: An Indispensable Material for Present and Future Applications. *Int. J. Polym. Sci.* **2020**, *2020*, 8834518. [CrossRef]
4. Bîrca, A.; Gherasim, O.; Grumezescu, V.; Grumezescu, A.M. Introduction in thermoplastic and thermosetting polymers. *Mater. Biomed. Eng. Thermoset Thermoplast. Polym.* **2019**, *10*, 1–28. [CrossRef]
5. Lunetto, V.; Galati, M.; Settineri, L.; Iuliano, L. Sustainability in the manufacturing of composite materials: A literature review and directions for future research. *J. Manuf. Process.* **2023**, *85*, 858–874. [CrossRef]
6. Fu, S.-Y.; Lauke, B.; Mai, Y.-W. *Science and Engineering of Short Fibre-Reinforced Polymer Composites*; Woodhead Publishing: Cambridge, UK, 2019. Available online: https://books.google.com/books/about/Science_and_Engineering_of_Short_Fibre_R.html?hl=it&id=fw2rDwAAQBAJ (accessed on 20 April 2026).
7. Köbler, J.; Schneider, M.; Ospald, F.; Andrä, H.; Müller, R. Fiber orientation interpolation for the multiscale analysis of short fiber reinforced composite parts. *Comput. Mech.* **2018**, *61*, 729–750. [CrossRef]
8. Abrate, S. The mechanics of short fiber-reinforced composites: A review. *Rubber Chem. Technol.* **1986**, *59*, 384–404. [CrossRef]
9. Jiang, L.; Zhou, Y.; Jin, F. Design of short fiber-reinforced thermoplastic composites: A review. *Polym. Compos.* **2022**, *43*, 4835–4847. [CrossRef]
10. Beaman, J.J.; Bourell, D.L.; Seepersad, C.C.; Kovar, D. Additive Manufacturing Review: Early Past to Current Practice. *J. Manuf. Sci. Eng. Trans. ASME* **2020**, *142*, 110812. [CrossRef]
11. Ahn, S.H.; Baek, C.; Lee, S.; Ahn, I.S. Anisotropic Tensile Failure Model of Rapid Prototyping Parts—Fused Deposition Modeling (FDM). *Int. J. Mod. Phys. B* **2012**, *17*, 1510–1516. [CrossRef]
12. Zohdi, N.; Richard (Chunhui), Y.; Torres-Giner, S.; Vargas, M. Material Anisotropy in Additively Manufactured Polymers and Polymer Composites: A Review. *Polymers* **2021**, *13*, 3368. [CrossRef] [PubMed]
13. *ASTM 52900:2021*; Additive Manufacturing—General Principles—Fundamentals and Vocabulary. British Standards Institution: London, UK, 2022.

14. Wang, Y.; Zhou, Y.; Lin, L.; Corker, J.; Fan, M. Overview of 3D additive manufacturing (AM) and corresponding AM composites. *Compos. Part A Appl. Sci. Manuf.* **2020**, *139*, 106114. [CrossRef]
15. Wang, X.; Jiang, M.; Zhou, Z.; Gou, J.; Hui, D. 3D printing of polymer matrix composites: A review and prospective. *Compos. B Eng.* **2017**, *110*, 442–458. [CrossRef]
16. Lunetto, V.; Galati, M.; Minetola, P.; Priarone, P.C. On the modelling of the specific energy consumption for the continuous fibre fabrication of composite materials. *Prog. Addit. Manuf.* **2024**, *10*, 5251–5268. [CrossRef]
17. Tănase, M.; Veres, C. Green Composites in Additive Manufacturing: A Combined Review and Bibliometric Exploration. *J. Manuf. Mater. Process.* **2025**, *9*, 301. [CrossRef]
18. Di Bella, G.; Puli, A.B.; Manjaiah, M.; Selvaraj, N.; Gokuldoss, P.K.; Joshi, A.G. Mechanical Response of FDM-Fabricated PEEK and Glass Fiber-Reinforced PEEK Under Varying Process Conditions. *J. Manuf. Mater. Process.* **2026**, *10*, 110. [CrossRef]
19. Markforged. Markforged Website. Available online: https://markforged.com/ (accessed on 13 April 2026).
20. Sekar, V.; Sellakumar, S.; Sivanesan, S. A comprehensive review of Markforged Onyx: Properties, applications, and future perspectives in 3D printing. *AIP Conf. Proc.* **2024**, *3161*, 020342. [CrossRef]
21. Pascual-González, C.; Iragi, M.; Fernández, A.; Fernández-Blázquez, J.P.; Aretxabaleta, L.; Lopes, C.S. An approach to analyse the factors behind the micromechanical response of 3D-printed composites. *Compos. B Eng.* **2020**, *186*, 107820. [CrossRef]
22. Peng, Y.; Wu, Y.; Wang, K.; Gao, G.; Ahzi, S. Synergistic reinforcement of polyamide-based composites by combination of short and continuous carbon fibers via fused filament fabrication. *Compos. Struct.* **2019**, *207*, 232–239. [CrossRef]
23. Benfriha, K.; Ahmadifar, M.; Shirinbayan, M.; Tcharkhtchi, A. Effect of process parameters on thermal and mechanical properties of polymer-based composites using fused filament fabrication. *Polym. Compos.* **2021**, *42*, 6025–6037. [CrossRef]
24. Sauer, M.J. Evaluation of the Mechanical Properties of 3D Printed Carbon Fiber Composites (Order No. 10789063). Available from ProQuest Dissertations & Theses Global. (2047544320). 2018. Available online: https://www.proquest.com/dissertations-theses/evaluation-mechanical-properties-3d-printed/docview/2047544320/se-2 (accessed on 13 April 2026).
25. Galati, M.; Viccica, M.; Minetola, P. A finite element approach for the prediction of the mechanical behaviour of layered composites produced by Continuous Filament Fabrication (CFF). *Polym. Test.* **2021**, *98*, 107181. [CrossRef]
26. Nikiema, D.; Balland, P.; Sergent, A. Study of 3D-printed onyx parts reinforced with continuous glass fibers: Focus on mechanical characterization, analytical prediction and numerical simulation. *J. Compos. Mater.* **2024**, *58*, 1717–1736. [CrossRef]
27. Naranjo-Lozada, J.; Ahuett-Garza, H.; Orta-Castañón, P.; Verbeeten, W.M.H.; Sáiz-González, D. Tensile properties and failure behavior of chopped and continuous carbon fiber composites produced by additive manufacturing. *Addit. Manuf.* **2019**, *26*, 227–241. [CrossRef]
28. Hou, Y.; Panesar, A. The moisture absorption of additively manufactured short carbon fibre reinforced polyamide. *Compos. Part A Appl. Sci. Manuf.* **2025**, *188*, 108528. [CrossRef]
29. Parmiggiani, A.; Prato, M.; Pizzorni, M. Effect of the fiber orientation on the tensile and flexural behavior of continuous carbon fiber composites made via fused filament fabrication. *Int. J. Adv. Manuf. Technol.* **2021**, *114*, 2085–2101. [CrossRef]
30. Canegrati, A.; Martulli, L.M.; Kostovic, M.; Rollo, G.; Sorrentino, A.; Carboni, M.; Bernasconi, A. Static Behavior of a 3D-Printed Short Carbon Fiber Polyamide: Influence of the Meso-Structure and Water Content. *Materials* **2024**, *17*, 1983. [CrossRef] [PubMed]
31. Moreno-Núñez, B.A.; Abarca-Vidal, C.G.; Treviño-Quintanilla, C.D.; Sánchez-Santana, U.; Cuan-Urquizo, E.; Uribe-Lam, E. Experimental Analysis of Fiber Reinforcement Rings' Effect on Tensile and Flexural Properties of OnyxTM–Kevlar® Composites Manufactured by Continuous Fiber Reinforcement. *Polymers* **2023**, *15*, 1252. [CrossRef] [PubMed]
32. Tosto, C.; Saitta, L.; Blanco, I.; Fichera, G.; Evangelista, M.; Jose, J.; Pantaleoni, A.; Bavasso, I. Additive Manufacturing of Carbon Fiber Cores for Sandwich Structures: Optimization of Infill Patterns and Fiber Orientation for Improved Impact Resistance. *J. Manuf. Mater. Process.* **2025**, *9*, 299. [CrossRef]
33. Dimitrellou, S.; Iakovidis, I.; Stratos, G.; Pagonis, D.N. Experimental Study on Sandwich Composites with Carbon Fiber Fabric Skin and 3D-Printed Carbon Fiber-Reinforced Polyamide Core. *J. Manuf. Mater. Process.* **2025**, *9*, 361. [CrossRef]
34. Mulholland, T.; Goris, S.; Boxleitner, J.; Osswald, T.A.; Rudolph, N. Fiber Orientation Effects in Fused Filament Fabrication of Air-Cooled Heat Exchangers. *JOM* **2018**, *70*, 298–302. [CrossRef]
35. Blok, L.G.; Longana, M.L.; Yu, H.; Woods, B.K.S. An investigation into 3D printing of fibre reinforced thermoplastic composites. *Addit. Manuf.* **2018**, *22*, 176–186. [CrossRef]
36. Inkson, B.J. Scanning electron microscopy (SEM) and transmission electron microscopy (TEM) for materials characterization. In *Materials Characterization Using Nondestructive Evaluation (NDE) Methods*; Woodhead Publishing: Cambridge, UK, 2016; pp. 17–43. [CrossRef]
37. JEOL. JEOL Website. Available online: https://www.jeol.com/ (accessed on 13 April 2026).
38. Quorum. Quorum Website. Available online: https://product.quorumtech.com/ (accessed on 13 April 2026).
39. Hermans, B.J.J.; Hermans, P.H.; Vermaas, D.; Weidinger, A. Quantitative Evaluation of Orientation in Cellulose Fibres from the X-ray Pibre Diagram. *Recl. Trav. Chim. Pays-Bas* **1946**, *65*, 427–447. [CrossRef]

40. Advani, S.G.; Tucker, C.L. The Use of Tensors to Describe and Predict Fiber Orientation in Short Fiber Composites. *J. Rheol.* **1987**, *31*, 751–784. [CrossRef]
41. ASTM. *Standard Test Method for Tensile Properties of Plastics*; ASTM: West Conshohocken, PA, USA, 2022. [CrossRef]
42. Nikiema, D.; Balland, P.; Sergent, A. Study of the Mechanical Properties of 3D-printed Onyx Parts: Investigation on Printing Parameters and Effect of Humidity. *Chin. J. Mech. Eng. Addit. Manuf. Front.* **2023**, *2*, 100075. [CrossRef]
43. EASYDUR. EASYDUR Website. Available online: https://www.easydur.com/ (accessed on 13 April 2026).
44. *ISO 527-1:2019*; Plastics—Determination of Tensile Properties—Part 1: General Principles. Available online: https://www.iso.org/standard/527-1 (accessed on 20 April 2026).
45. Tescan. Tescan Website. Available online: https://tescan.com/ (accessed on 3 June 2026).
46. AGAR SCIENTIFIC. AGAR SCIENTIFIC Website. Available online: https://www.agarscientific.com/ (accessed on 3 June 2026).
47. Scott, D.W. Sturges' rule. *WIREs Comp. Stat.* **2009**, *1*, 303–306. [CrossRef]
48. Bunsell, A.R.; Joannès, S.; Marcellan, A. Testing and characterization of fibers. In *Handbook of Properties of Textile and Technical Fibres*; Woodhead Publishing: Cambridge, UK, 2018; pp. 21–55. [CrossRef]
49. Ogierman, W.; Kokot, G. A study on fiber orientation influence on the mechanical response of a short fiber composite structure. *Acta Mech.* **2016**, *227*, 173–183. [CrossRef]
50. Jeppesen, N.; Mikkelsen, L.P.; Dahl, A.B.; Christensen, A.N.; Dahl, V.A. Quantifying effects of manufacturing methods on fiber orientation in unidirectional composites using structure tensor analysis. *Compos. Part A Appl. Sci. Manuf.* **2021**, *149*, 106541. [CrossRef]
51. Li, Y.; Stier, B.; Bednarcyk, B.; Simon, J.W.; Reese, S. The effect of fiber misalignment on the homogenized properties of unidirectional fiber reinforced composites. *Mech. Mater.* **2016**, *92*, 261–274. [CrossRef]
52. Jena, S.R.; Agarwal, S.; Sivanandam, S.; Gamini, S.; Rohini, D.; Phani Sai kumar, N.V. AI-driven multiphysics modelling for optimizing fiber dispersion in thermoplastic and thermosetting polymer composites for additive manufacturing. *Therm. Sci. Eng. Prog.* **2025**, *59*, 103304. [CrossRef]
53. Wu, F.; Grohmann, C.; Ji, F.; Cai, Z.; Yang, L.; Bartolo, P.; Mirihanage, W. Controlling microstructure formation in metal additive manufacturing via deep learning driven spatiotemporal temperature regulation. *Prog. Addit. Manuf.* **2026**, *11*, 2285–2294. [CrossRef]

https://doi.org/10.3390/jmmp10060210